# Influence of mean circulation on large-scale decadal basin modes

by Dhouha Ferjani[1], Thierry Huck[2], and Alain Colin de Verdière[2]

## ABSTRACT

The effect of large-scale mean circulation on the generic property of intrinsic basin modes of decadal variability is investigated through linear stability analysis of a two-layer shallow water model over a flat- and a variable-bottom topography. The mean circulation is forced through either surface wind stress or vertical velocities at the layers interface representing surface heat flux. Regardless of the type of forcing, the large-scale mean circulation reduces the damping of the decadal basin modes. The wind forcing mostly affects the mode damping, by up to 30% for a climatological amplitude, whereas the heat flux forcing mostly increases the oscillation period, by several years (up to 30%). The oscillation period, characteristic of the adjustment process to the steady mean flow, displays, however, different behavior depending on the meridional shift of the eastward barotropic advection in the region of maximum basin mode amplitude: The period gets shortened (lengthened) in the wind-forced (thermally forced) experiment with respect to the unforced one. The results are rationalized through the analysis of long Rossby waves propagation and underscore the key role of two processes in setting the oscillation period of the basin adjustment: (1) changes in Rossby wave speed due to changes in isopycnals depth and (2) changes in the mean barotropic zonal flow. These processes reinforce each other in the thermal-forcing case, resulting in large modifications of the mode period, but almost compensate in the wind-forced case, resulting in slight changes of the mode period, compared with the reference rest state.

*Keywords.* stationary circulation, wind forcing, thermal forcing, linear stability analysis, basin modes, oscillation period

## 1. Introduction

A rich spectrum of interannual to multidecadal climate variability appears in modern climate data (Levitus 1989; Deser and Blackmon 1993; Kushnir 1994; Hansenand Bezdek 1996; Reverdin, Cayan and Kushnir 1997; Sutton and Allen 1997; Delworth and Mann 2000). Understanding the natural variability in the climate system is important for both short-term climate prediction and credible long-term projection of global climate change. Large-scale, low-frequency ocean oscillations are believed to play an essential role in natural

---

1. Corresponding author address: Laboratoire de Physique des Océans, Université de Bretagne Occidentale, UFR Sciences, 6 avenue Le Gorgeu, BP 809, 29285 Brest cedex, France. *e-mail: dhouha.ferjani@univ-brest.fr*
2. Laboratoire de Physique des Océans (UMR 6523 CNRS IFREMER IRD UBO), Brest, France.

climate variability on a broad range of timescales. The adjustment is achieved through nondispersive, baroclinic planetary waves that cross the ocean basin in years to tens of years at midlatitude. The standard linear theory for such waves in enclosed basins has been explored (Cessi and Louazel 2001; Cessi and Primeau 2001; Yang and Liu 2003), and much is now understood about basin modes in reduced-gravity oceans at rest. However, the relevance of such modes to explain the variability found in observations and realistic ocean or coupled models simulations is still to be proved: Weijer et al (2013), for instance, have examined this issue for the North Pacific, with no success. It is then particularly critical to extend basin modes theory to more realistic configurations and forcing.

Most of the studies examined the low-frequency, large-scale basin modes as prototypes for interdecadal oscillation of the basin adjustment process from a quasigeostrophic (QG) perspective (LaCasce 2000; Cessi and Primeau 2001; Spydell and Cessi 2003; Ben Jelloul and Huck 2003, 2005). Other studies carried out in shallow-water (SW) models considered flat-bottom oceans and reduced gravity configurations (Cessi and Louazel 2001; LaCasce and Pedlosky 2002; Primeau 2002). The aim of this article is to continue this line of investigation by considering the joint influence of the background mean circulation and bottom topography on the decadal basin modes. Recently, Ferjani, Huck, and de Verdière (2013) assessed the influence of bottom topography on the baroclinic basin modes that develop within a rest state: they found an additional baroclinic decay through energy conversion to barotropic modes that remains weak compared with frictional processes. However, this conclusion has to be tested when thermodynamic or mechanical stationary forcing drives a mean circulation in order to assess the robustness of the decadal variability in more realistic model configurations. The influence of a mean flow on Rossby wave propagation fundamentally depends on their respective vertical structure, leading either to non-Doppler shift effect when both have the same vertical structure (Held 1983; Liu 1999; de Verdière Tailleux 2005) or Doppler shift, as for the influence of a barotropic flow on the first baroclinic mode (Klocker and Marshall 2014).

To address this topic in the simplest manner, we use here a two-layer SW model, under either steady wind or thermal forcing, in order to characterize the large-scale, wavelike response in a closed ocean basin. This model formulation allows also for a latitudinal variation of the Rossby radius, which is important for the decadal variability of the ocean circulation. We have chosen to focus on the large-scale regime because of its importance for the observations of low-frequency oceanic variability. The mean circulation consists of a Sverdrup flow for the double gyre wind-driven experiments and a purely baroclinic flow for the zonally uniform thermal-forcing experiments. The equations are linearized for perturbations around a background steady state, and the linear stability analysis of the Jacobian matrix is performed in order to extract the least damped modes structure, decay time, and oscillation period. The latter is found to be set by the propagation of general potential vorticity (PV) Rossby waves across the basin at the latitude of maximum variability amplitude, suggesting that these general waves, analogous to the classical planetary Rossby waves but modified by the mean circulation, are the most likely candidate to explain the signature of large-scale interdecadal variability.

The material is organized as follows: the model and configuration are described in Section 2; the equations for the advection of perturbations by the mean flow are derived analytically in Section 3. Section 4 discusses the effect of different types and magnitudes of the forcing on the decadal mode of variability, and Section 5 provides some conclusions.

## 2. Formulation and model description

### a. Shallow-water model equations

Although the QG models are useful tools in understanding the general ocean circulation, they ignore some important aspects of the dynamics—namely the nonlinearity associated with layer thickness change and the full variation of the Coriolis parameter $f$. As a consequence, numerical QG solutions for a double gyre basin (Holland 1978) show patterns having the mirror symmetry of the forcing and a Gulf Stream–like midlatitude jet, located around the zero wind-stress-curl line. Huang (1986) shows that this mirror symmetry disappears as soon as the layer thickness change becomes large leading to a strongly nonlinear Gulf Stream–like interior boundary current, even if the inertial terms are ignored.

On large scales, the Coriolis parameter, the geographic variation of the basic stratification, and the large-amplitude topography cannot be neglected. This motivates the choice of the SW formulation, whose simplest form equations are given by the planetary geostrophic approximation that neglects the nonlinear momentum advection terms. The latter is justified for scales large compared with the internal Rossby radius. However, deviating from the planetary geostrophic approximation, we retain the local time derivative in the horizontal momentum for numerical reasons linked to time integration and linear stability analysis (i.e., we allow for gravity waves and short Rossby waves in addition to long Rossby waves). Such a formulation has already been used in the BARBI model (Eden and Olbers 2010) for instance. The continuous stratification in the real ocean is modeled hereafter as two immiscible layers with an upper layer representing the light water above the main thermocline, and a lower layer about three times thicker than the upper one.

The system is assumed to be dissipated by lateral friction, and frictional effects at the bottom and at layer interfaces are absent. The enclosed Cartesian β-plane ocean basin $D = \{0 \leq x \leq L_x, -L_y/2 \leq y \leq L_y/2\}$ is centered at 45° N, extending from 15° N to 75° N, and 60° wide in longitude. The coordinates $(x, y)$ are positive eastward and northward. The Coriolis parameter $f$ is linearized about the reference latitude (45° N) so that $f = f_0 + \beta y$. The Boussinesq two-layer SW equations can be written as follows:

$$\partial_t \mathbf{u_i} + f\mathbf{k} \times \mathbf{u_i} = -\nabla \left[ g\eta_1 + \delta_{i2} g'(\eta_2 - \eta_1) \right] + \nu\nabla^2 \mathbf{u_i} + \delta_{i1} \frac{\tau}{\rho_0 h_i}, \qquad (1a)$$

$$\partial_t h_i + \nabla \cdot (h_i \mathbf{u_i}) = (-1)^{(i-1)} w_I. \qquad (1b)$$

The notation is standard; that is, $h_i$, $\mathbf{u_i}$ denote the thickness and velocity of each layer $i = 1, 2$ and compose the state vector for which we have to solve. The unit vector $\mathbf{k}$
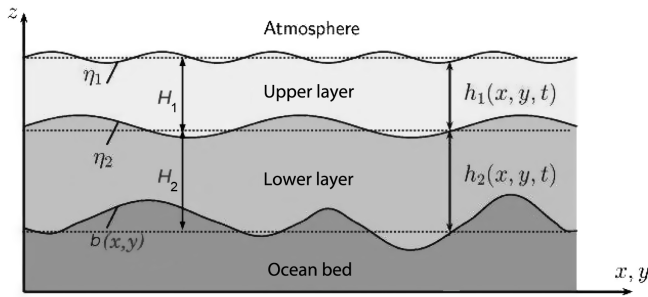
Figure 1. Schematic structure of the two-layer shallow-water ocean model and notations.

points upward, $\delta_{ij}$ is the Kronecker delta operator, $\rho_i$ is the density in each layer, $g$ is the acceleration due to gravity, and $g' = g\frac{\rho_2-\rho_1}{\rho_2}$ is the reduced gravity.

We denote by $\eta_1$ the free surface elevation and $\eta_2$ the interface displacement with respect to the undisturbed fluid thicknesses $H_i$ (Fig. 1). They are related to the total layer thicknesses by $h_1 = H_1 + \eta_1 - \eta_2$ and $h_2 = H_2 + \eta_2 - b$, such that $h(x, y, t) = h_1 + h_2 = H_0 + \eta_1(x, y, t) - b(x, y)$ corresponds to the total fluid layer thickness, with $H_0 = H_1 + H_2$ the constant undisturbed fluid thickness; $b(x, y)$ is the bottom topography height above the level surface lying at the bottom of the second layer.

Similarly to Ferjani, Huck, and de Verdière (2013), the divergence of the horizontal momentum flux due to mesoscale eddies is parametrized through a Laplacian horizontal viscosity, appropriate for scales larger than the deformation radius. The frictional transfer of momentum in the vertical direction, except for the wind stress $\tau$ (N m$^{-2}$), is neglected, and there is no diffusion term in the continuity equations. The thermal forcing $w_I$ that appears under the form of a vertical velocity imposed at the layer interface is detailed in Section 2b. Hence, equations (1a) and (1b) form the forced version of the model used by Ferjani, Huck, and de Verdière (2013), to address the influence of bottom topography on decadal basin modes.

Given that the horizontal resolution $\Delta x$ is large compared with the oceanic internal Rossby radius, we follow current practice to determine the viscosity coefficient as a function of the resolution: $\nu \approx 1.6\beta\Delta x^3$ (m$^2$ s$^{-1}$) to ensure that it correctly resolves Munk's boundary layer. Although the implied friction coefficient is large, interior flows of scale $L$ are geostrophic to order Ekman number $\nu/fL^2$. For $L$ of order 1,000 km, this number is less than 1% for the values used here. Such values along with those appended in Table 1 are typical for the North Atlantic basin and used as pivots on which the present work is built. Lateral boundaries are impermeable; that is, $\mathbf{u} \cdot \mathbf{n} = 0$, with $\mathbf{n}$ the vector normal to solid walls to ensure mass conservation, and no-slip boundary conditions are imposed on the lateral solid walls.

Sensitivity tests to topographic heights are carried out by implementing a Gaussian shaped midocean ridge (MOR) in the zonal direction centered in the middle of the basin that will

Table 1. Typical parameters for the experiment in the linear shallow-water model.

| Symbol | Value | Description |
|---|---|---|
| $f_0$ | $10^{-4}$ s$^{-1}$ | Coriolis parameter at $y = 0$ (45° N) |
| $\beta$ | $1.6 \times 10^{-11}$ m$^{-1}$ s$^{-1}$ | Meridional gradient of Coriolis parameter |
| $L_x$ | $6.6 \times 10^6$ m | Basin zonal extent |
| $L_y$ | $6.6 \times 10^6$ m | Basin meridional extent |
| $H_1$ | 1,000 m | Upper-layer mean depth at rest |
| $H_2$ | 3,000 m | Bottom-layer mean depth at rest |
| $H_0$ | $H_1 + H_2$ | Total mean depth at rest |
| $\rho_0$ | 1,023 kg m$^{-3}$ | Mean density |
| $g$ | 9.81 m s$^{-2}$ | Gravity acceleration at Earth's surface |
| $g' = g\Delta\rho/\rho_0$ | $2 \times 10^{-2}$ m s$^{-2}$ | Reduced gravity acceleration |
| $\nu$ | $10^5$ m$^2$ s$^{-1}$ | Laplacian eddy viscosity |
| $n_x \times n_y$ | $60 \times 60$ | Number of grid points in the horizontal |
| $\alpha$ | $0.2 \times 10^{-3}$ K$^{-1}$ | Thermal expansion coefficient |
| $C_p$ | $4 \times 10^3$ J kg$^{-1}$ K$^{-1}$ | Water heat capacity |
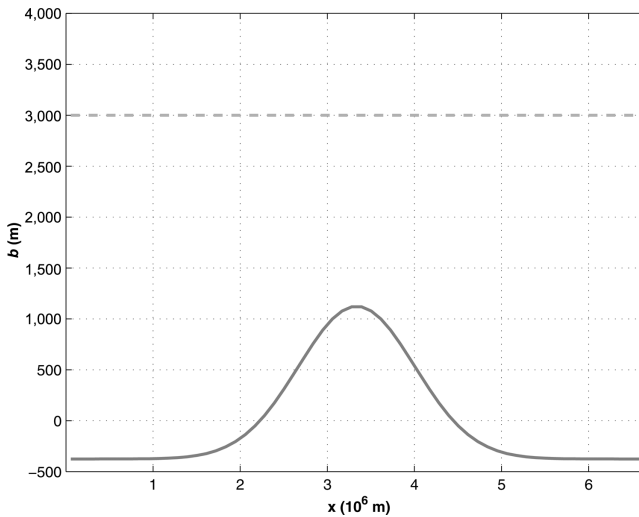


Figure 2. Profile of the analytical topography (solid line), corresponding to 1,500 m amplitude height. The dashed line denotes the interface level at rest measured from the undisturbed bottom-layer thickness $H_2$.

disturb westward propagation of Rossby waves (Fig. 2). Results are compared with the flat-bottom experiment taken as a reference case. The Gaussian width of the bottom elevation is approximately one-third of the basin zonal extent with a height spanning from 0 to 1,500 m. The bottom depth is adjusted such that the basin volume remains constant.

For small disturbances of a stratified background mean flow state $(\overline{h_i}, \overline{\mathbf{u_i}})$, the linearized equations of (1a) and (1b) are obtained for the perturbed layer thicknesses $h_1' = \eta_1' - \eta_2'$ and $h_2' = \eta_2'$ as follows:

$$\partial_t \mathbf{u_i'} + f\mathbf{k} \times \mathbf{u_i'} = -\nabla\left[g(h_1' + h_2') - \delta_{i2}g'h_1'\right] + \nu\nabla^2\mathbf{u_i'}, \tag{2a}$$

$$\partial_t h_i' + \nabla \cdot \left(\overline{h_i}\mathbf{u_i'}\right) + \nabla \cdot \left(h_i'\overline{\mathbf{u_i}}\right) = 0. \tag{2b}$$

### b. Forcing

The wind-driven simulations are forced by applying a zonal, cosine-shaped wind stress $\tau(x, y) = \tau_0 \cos(2\pi y/L_y)$, with a maximum in the middle of the basin and minima at the northern and southern boundaries, leading to a double gyre circulation. The numerical experiments are carried out with forcing values ranging up to climatological amplitudes (typically 0.1 N m$^{-2}$), but sufficiently low to prevent layer outcropping.

The thermally forced experiments are driven by a purely baroclinic buoyancy forcing. A simple way of representing the heat flux $Q$ (in W m$^{-2}$) at the ocean surface (positive into the ocean) is to impose an equivalent volume transfer between the two layers of distinct densities, that is, a vertical velocity $w_I = Q\alpha/(C_p\Delta\rho)$ at the layer interface, in the mass conservation equation where $\alpha$ is the thermal expansion coefficient and $C_p$ the water specific heat capacity. Veronis (1978) assumed a uniform upwelling within the interior and a line sink along the northern wall. In the present model, $w_I$ is assumed to be a linear function of latitude, changing from an upwelling in the subtropical basin (warming) to a downwelling in the subpolar basin (cooling).

### c. Nonlinear integrations

The numerical solution is obtained by discretizing the model equations and integrating forward in time with the leapfrog scheme (with a time step $\Delta t = 100$ s) over 40 years, starting from rest (uniform layer depths). The computational mode of the leapfrog scheme is damped with a three-point Asselin time filter. The spatial discretization is based on finite difference second-order centered schemes for advection and diffusion, on a regular Arakawa C-grid with 60 points in each direction.

The forced experiments driven either by wind stress or heat flux, with a flat- or variable-bottom topography, reach steady states that serve as a starting point to perform linear stability analyses to explore the combined effect of a mean flow and topography on low-frequency basin modes. Figure 3 displays such a climatologically forced double gyre stationary circulation. The wind-forced mean flow patterns (Fig. 3, left) show an anticyclonic subtropical gyre connected to a cyclonic subpolar gyre via a midlatitude eastward top-trapped jet, whose zonal extension depends on the forcing magnitude. With the addition of an MOR (Fig. 4), the mean flow in layer 2 remains weak and the influence of topography negligible. Remember that the momentum advection terms are absent and therefore the effect of geostrophic
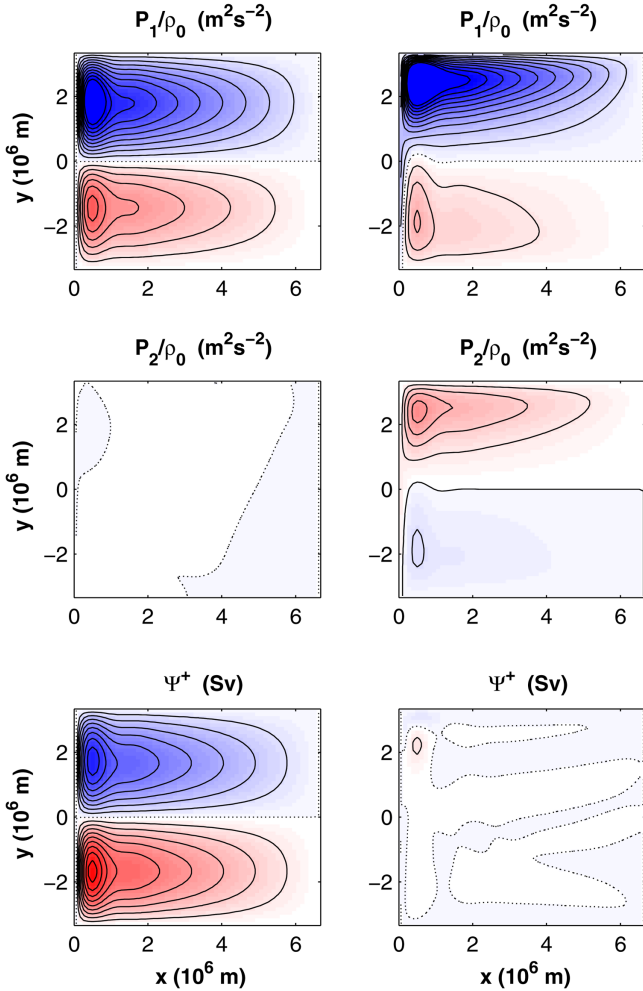
Figure 3. Wind-forced (left) and thermally-driven (right) steady circulation under a climatological-forcing magnitude ($\sim 30$ m y$^{-1}$) in the flat-bottom experiment: the pressure in each layer is defined in equation (1a) as $p_i = g\eta_1 + \delta_{i2}g'(\eta_2 - \eta_1)$, divided by $\rho_0$ (contour interval 0.5 m$^2$ s$^{-2}$) (top, middle); the barotropic streamfunction (contour interval 5 Sv) (bottom). Negative contours are dashed, positive contours are solid, and the zero contour is dotted.

eddies to create deep mean flow. Because outcropping is not allowed, no direct wind forcing can excite the deep layer either. The gyres are not exactly antisymmetric about the zero-wind-stress-curl line so that the circulation is not internally compensated, as the input of anticyclonic vorticity in the southern (subtropical) gyre is not exactly balanced by an input of cyclonic vorticity in the northern (subpolar) gyre. The net flux of vorticity is expelled through the boundaries of the basin via frictional processes.
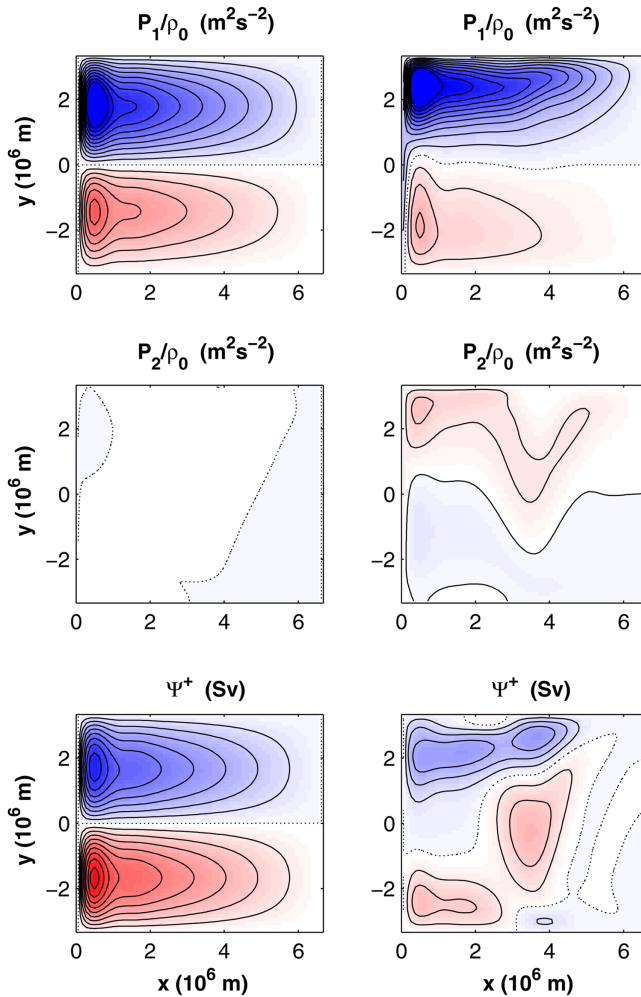
Figure 4.  Same as in Figure 3 for the experiment with a 1,000 m height midocean ridge topography.

The circulation driven by the differential heating (right panel of Fig. 3, right) shows similar patterns with an anticyclonic subtropical gyre in the upper layer and a deep water formation in the northwest corner feeding the opposite circulation at depth. Conversely, it shows a subpolar gyre strongly intensified along the northern boundary (where the forcing field reaches its maximum), within which tighter meridional pressure gradients are observed. Furthermore, with equal forcing amplitude, it displays nonzero steady barotropic streamfunction in the presence of topography (Fig. 4, right), which becomes vanishingly small in the flat-bottom experiment. This barotropic circulation is of the same order as for

the wind-forced experiment, but entirely due to the strong interaction of the baroclinic flow with the bottom topography.

### d. Linear stability analysis

When the steady state is reached, the linear stability analysis of the solution is performed to examine the evolution of perturbations (free waves) about this background steady state $\overline{X}$. The linearized prognostic equations (2a) and (2b) of our model can be written for the perturbation $X$ as a general dynamical system:

$$\partial_t X = J X, \tag{3}$$

where $X = (h_i, \mathbf{u}_i)$ is the state vector, and the Jacobian matrix, $J$, is function of the steady state $\overline{X}$. Assuming that the solution has a wavelike form,

$$X = \begin{bmatrix} h_i \\ \mathbf{u_i} \end{bmatrix} (x, \ y, \ t) = e^{\omega t} \begin{bmatrix} \hat{h}_i \\ \hat{\mathbf{u}}_\mathbf{i} \end{bmatrix} (x, \ y), \tag{4}$$

the eigenvalue problem of the perturbations—namely, $\omega X = J X$—is resolved to determine the eigenvalues $\omega$ and associated eigenvectors of the Jacobian built up on the mean flow. Two methods have been implemented, one based on the explicit Jacobian of the model and the other on the linear tangent model. In the first case, the Jacobian matrix of the linear system is explicitly computed. Its leading eigenvalues (typically 30) based on the largest real part are computed using Arnoldi's method as provided in ARPACK (Lehoucq, Sorensen, and Yang 1998). This method is limited by the size of the explicit Jacobian matrix that must fit in the computer memory. In the second case, the tangent linear model is used to compute the leading eigenvalues of the propagator $M(\tau)$ over a "short" integration time ($\tau = 0.1$ y here) with ARPACK:

$$X(t = \tau) = M(\tau) \, X(t = 0) = e^{J\tau} X(t = 0), \tag{5}$$

where the initial perturbations $X(t = 0)$ are provided by the Arnoldi method. The Jacobian eigenvalues $\omega$ are then deduced from the propagator eigenvalues $e^{\omega \tau}$. We checked that the results are not sensitive to the integration time $\tau$ over a large range of values, small compared with the baroclinic Rossby waves basin crossing time but large with respect to the gravity waves basin crossing time. The latter method is much more efficient as it avoids the computation of the explicit Jacobian matrix, allowing a much larger number of model grid points (up to 300 points in each direction).

Unless otherwise specified, our solutions are obtained in an idealized basin with the typical parameters listed in Table 2. Linear stability calculations are performed for the forced experiments in the case of a flat-bottom and a 1,000 m meridional ridge. In all cases, the eigenvalues display a negative real part demonstrating stability. We focus interest on those having the smallest negative real part and hence the most weakly damped modes: their nonzero imaginary part leads to oscillation periods of decades.

Table 2. First eigenvalue of the Jacobian matrix under different forcing (wind and heat flux) of a
  climatological magnitude, along with the unforced reference experiment. The damping timescale
  is defined as $\tau = 1/\omega_r$, and the oscillation period $T = 2\pi/\omega_i$. MOR, midocean ridge.

| Forcing | Topography | $\omega_r$ $(\mathrm{y}^{-1})$ | $\omega_i$ $(\mathrm{y}^{-1})$ | $\tau$ (y) | $T$ (y) |
|---------|-----------|------------|------------|--------|--------|
| None    | Flat      | −0.202     | 0.365      | −4.93  | 17.21  |
|         | MOR       | −0.220     | 0.413      | −4.54  | 15.18  |
| Wind    | Flat      | −0.147     | 0.386      | −6.77  | 16.22  |
|         | MOR       | −0.167     | 0.409      | −5.98  | 15.31  |
| Thermal | Flat      | −0.184     | 0.278      | −5.41  | 22.60  |
|         | MOR       | −0.212     | 0.331      | −4.70  | 18.94  |

## 3. Influence of the mean flow on the perturbations

Our intent is to show explicitly the terms that drive the propagation of perturbations in
the thermocline. For each variable, we note $X^+$ the vertically averaged component, $hX^+ =
h_1 X_1 + h_2 X_2$, and $X^- = X_1 - X_2$ its baroclinic counterpart, so that $X_1 = X^+ + \frac{h_2}{h} X^-$
and $X_2 = X^+ - \frac{h_1}{h} X^-$.

### a. The geostrophic form of the equations

With planetary geostrophy, the unforced vorticity equation in each layer $i$ is reduced to
the following:

$$\beta v_i + f \nabla \cdot \mathbf{u_i} = 0. \tag{6}$$

Then the continuity equation for layer 1 becomes

$$\partial_t (\eta_1 - \eta_2) - \mathbf{u_1} \cdot \nabla \eta_2 - \frac{\beta h_1}{f} v_1 = 0, \tag{7}$$

where $\mathbf{u_1} \cdot \nabla \eta_1$ cancels from the upper-layer geostrophy, while for layer 2,

$$\partial_t \eta_2 + \mathbf{u_1} \cdot \nabla \eta_2 - \mathbf{u_2} \cdot \nabla b - \frac{\beta h_2}{f} v_2 = 0, \tag{8}$$

using $\mathbf{u_2} \cdot \nabla \eta_2 \approx \mathbf{u_1} \cdot \nabla \eta_2$ from the thermal wind balance to $O(\Delta \rho/\rho)$. Refer to the Appendix
for the detailed derivation of these equations. Adding these two equations gives

$$\beta h v^+ = f \partial_t \eta_1 - f \mathbf{u_2} \cdot \nabla b. \tag{9}$$

This reduces to the topographic Sverdrup relation when the first term on the right-hand side
is neglected (the rigid-lid approximation).

When velocities $\mathbf{u_i}$ are written in terms of $\mathbf{u}^+$ and $\mathbf{u}^-$ in equations (8) and (9), with the help of geostrophy and after simple algebra using equation (7), the following equations are obtained:

$$\partial_t \eta_1 - \frac{\beta h}{f} v^+ - \mathbf{u}^+ \cdot \nabla b - \frac{g' h_1}{fh} J(\eta_2, b) = 0, \tag{10}$$

$$\partial_t \eta_2 + (\mathbf{u}^+ + c_R \mathbf{i}) \cdot \nabla \eta_2 + \frac{\beta h_1}{f} v^+ = 0, \tag{11}$$

where $c_R$ is the traditional zonal phase speed of the baroclinic Rossby wave:

$$c_R = -\frac{\beta}{f^2} g' \frac{h_1 h_2}{h}, \tag{12}$$

with $\mathbf{i}$ the zonal unit vector and $J(A, B) = \partial_x A \partial_y B - \partial_y A \partial_x B$ the Jacobian operator. $J(\eta_2, b)$ is often referred to as the joint effect of baroclinicity and relief (JEBAR) term: details and references are given in Ferjani, Huck, and de Verdière (2013). These two coupled equations in $(\eta_1, \eta_2)$ allow us to calculate the interaction of geostrophic motions with topography. If the rigid-lid approximation is carried out, equation (10) is not prognostic anymore, and a streamfunction can be introduced as follows:

$$h\mathbf{u}^+ = \mathbf{k} \times \nabla \psi^+, \tag{13}$$

so that

$$J\left(\psi^+, \frac{f}{h}\right) = g' \frac{h_1}{h^2} J(b, \eta_2). \tag{14}$$

This is the familiar Sverdrup form, which demonstrates how the JEBAR term on the right can induce a barotropic flow across PV contours.

Using equation (14), the last term in equation (11) becomes

$$\frac{\beta h_1}{f} v^+ = \frac{h_1}{h} \mathbf{u}^+ \cdot \nabla h + \frac{g' h_1^2}{fh^2} J(b, \eta_2). \tag{15}$$

A second form of the governing equation for the interface $\eta_2$ results as follows:

$$\partial_t \eta_2 + (\mathbf{u}^+ + c_R \mathbf{i}) \cdot \nabla \eta_2 - \frac{h_1}{h} \mathbf{u}^+ \cdot \nabla b + \frac{g' h_1^2}{fh^2} J(b, \eta_2) = 0, \tag{16}$$

where $c_R$ is the previously defined zonal Rossby wave speed. Equation (16) is an extension of the long nonlinear Rossby wave propagation equation (3.13) derived by Schopp (1988) for a flat-bottomed ocean. The presence of topography adds the last two terms in equation (16). In the absence of topography, Schopp (1988) demonstrates the importance of the arrested wave condition (when $u^+ = -c_R$).

The variations of $c_R$ with layer thickness in equation (16) also predict that a finite amplitude anomaly can develop fronts (Dewar 1987; Schopp 1988). With topography, a barotropic perturbation with the form of a dipole extends pseudowestward as soon as an eddylike anomaly propagating from the eastern boundary feels the varying bottom topography: the baroclinic anomaly deforms and decreases over the topography as shown by Sakamoto and Yamagata (1997).

These nonlinearities in the problem that appear under the form of steepening terms (wave speed dependence on signal amplitude) contribute to couple the dynamics in the two layers. However, aside from the nonlinear coupling, the system equations (14) and (16) shows that the barotropic and baroclinic responses are coupled by the topography. Indeed, there is a strong feedback loop between the barotropic and the baroclinic flow that initially created it. This feedback stems from a linear, topographic coupling of the fast barotropic and slow baroclinic waves of the system. The evolution of $\eta_1$ and $\eta_2$ in equations (10) and (11) cannot be decoupled even in their linearized form.

### b. Linearized equations

In order to analyze the mean flow influence on the modes, we now linearize these equations around a steady state $\overline{\mathbf{X}} = \mathbf{X} - \mathbf{X}'$, where $\mathbf{X}'$ represents the perturbation. We introduce the equivalent depth $h^* = \frac{h_1 h_2}{h}$ appearing in the definition of the long Rossby wave speed equation (12), which we can alternatively write as $c_R = g' h^* \partial_y \left( \frac{1}{f} \right)$. Linearizing $h^*$ gives

$$\overline{h^*} + h^{*'} \approx \frac{\overline{h_1 h_2}}{\overline{h}} + \frac{\overline{h_2 - h_1}}{\overline{h}} h_1' \approx \frac{\overline{h_1 h_2}}{\overline{h}} - \frac{\overline{h_2 - h_1}}{\overline{h}} \eta_2', \tag{17}$$

which results from $h_1' = -h_2' = -\eta_2'$ as $\eta_1'$ vanishes in the rigid-lid limit. Linearizing $c_R$ now gives

$$\overline{c_R} + c_R' \approx g' \overline{h^*} \, \partial_y \left( \frac{1}{f} \right) + g' h^{*'} \, \partial_y \left( \frac{1}{f} \right). \tag{18}$$

With these notations, the linearization of equation (16) provides

$$\partial_t \eta_2' + (\overline{\mathbf{u}^+} + \overline{c_R}\mathbf{i}) \cdot \nabla \eta_2' + (\mathbf{u}'^+ + c_R'\mathbf{i}) \cdot \nabla \overline{\eta_2} + \frac{\eta_2'}{\overline{h}} \overline{\mathbf{u}^+} \cdot \nabla b - \frac{\overline{h_1}}{\overline{h}} \mathbf{u}'^+ \cdot \nabla b$$

$$- \frac{2g' \overline{h_1} \eta_2'}{f \overline{h}^2} J\left(b, \overline{\eta_2}\right) + \frac{g' \overline{h_1}^2}{f \overline{h}^2} J\left(b, \eta_2'\right) = 0. \tag{19}$$

To interpret the influence of the mean flow on the modes period, we will focus in the next section on the first two terms that propagate interface perturbations in the zonal direction through the long Rossby waves (at speed $\overline{c_R}$, based on the mean state layer thickness $\overline{h^*}$) and through the mean barotropic velocity $\overline{\mathbf{u}^+}$, respectively. All the remaining terms
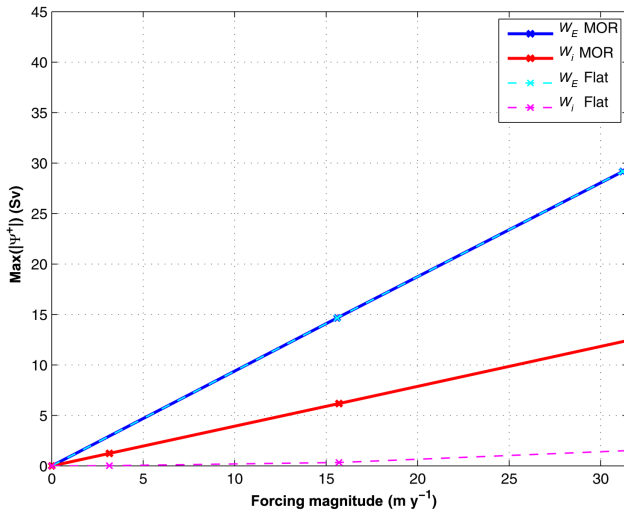
Figure 5. Maximum of the barotropic streamfunction as function of the forcing type (wind, $w_E$; heat flux, $w_I$) and magnitude (m y$^{-1}$), in the presence (solid) or not (dashed) of a 1,000 m midocean ridge (MOR). In the climatological range, the upper-layer thickness does not vanish, inhibiting the Ekman pumping to penetrate the lower layer and to put it into motion. Hence, the Sverdrup circulation (blue) does not "feel" the presence of the bottom topography. Note that the interaction of the baroclinic thermal forcing with the bottom ridge (red) leads to a barotropic circulation almost half of the Sverdrup flow.

involve either source/sink terms proportional to $\eta_2'$ or barotropic velocity anomalies $\mathbf{u}'^+$ that instantaneously adjust to the interface perturbations due to infinite barotropic Rossby waves phase speed ($h\mathbf{u}^{+'} = \mathbf{k} \times \nabla \psi'^+$). Note that the last topographic term in equation (19) advects perturbations meridionally, southward (northward), respectively east (west) of the ridge topography (MOR).

## 4. Influence of the mean flow on basin modes

Stationary circulations are computed for increasing forcing magnitudes in terms of Ekman pumping, $w_E = \mathbf{k} \cdot \nabla \times \tau / (\rho_0 f)$ (m s$^{-1}$), and thermal flux, $w_I$ (m s$^{-1}$), as control parameters, all lying within the climatological range (Fig. 5). With a variable-bottom topography, the differential heat forcing, varying linearly in latitude from 40 W m$^{-2}$ at 15° N to −40 W m$^{-2}$ at 75° N, corresponds to a downward diapycnal flux of 31.5 m y$^{-1}$ in the northern half of the basin, forcing an overturning circulation of about 11 Sv and leading to a maximum barotropic streamfunction of about 12 Sv. This barotropic circulation is built up by the interaction of the baroclinic vorticity injected by the thermal forcing with the topography, in contrast with the flat-bottom experiment where the maximum $|\Psi^+|$ of the thermally forced circulation is nearly zero. In the wind-forced experiments, a zonal wind stress of
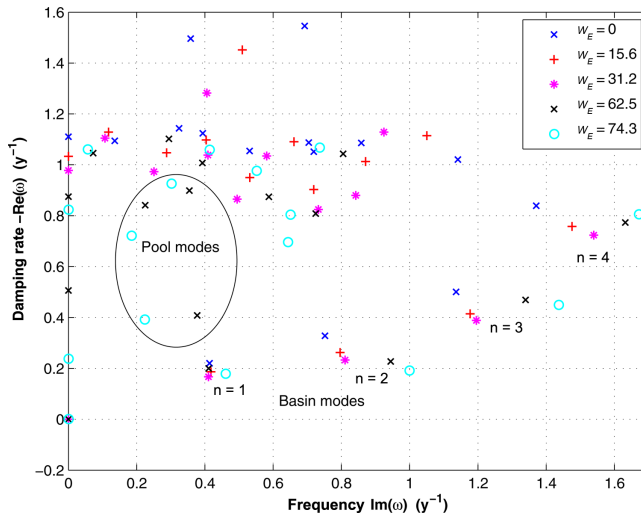
Figure 6. Eigenvalue spectrum under increasing strength of the wind forcing in the case of a 1,000 m height midocean ridge experiment. Apart from the presence of the classical basin modes (zonal wavenumber n = 1, and higher wavenumbers to the right), note the emergence of a new class of lower-frequency modes, the oscillatory pool modes, trapped within closed geostrophic contours (Ferjani, 2013), that only appear at large forcing magnitude when the westward Rossby waves are arrested by the mean flow.

a climatological magnitude $O(0.1 \text{ N m}^{-2})$, corresponding to an upwelling in the subpolar gyre of 31.2 m $y^{-1}$, leads to an increased maximum $|\Psi^+|$ up to 30 Sv.

For each forcing magnitude, the computed steady state is introduced in the linear stability analysis that provides the frequency, decay rate, and spatial pattern of the perturbation modes. Despite the presence of an MOR of 1,000 m height, the basin modes eigenspectrum remains similar to the QG ones that appear during the Sverdrup adjustment as described by Spydell and Cessi (2003) over a flat bottom, and by Ben Jelloul and Huck (2005) with a reduced gravity model. Under the climatological wind-forcing magnitude, the eigenspectrum displays large-scale low-frequency classical baroclinic basin modes weakly modified by Doppler shifting by the barotropic flow. The emergence of a new class of pool modes with lower frequencies, entirely confined in closed geostrophic contours, appears only at strong forcing magnitudes when the PV Rossby waves are arrested by the mean flow. Figure 6 shows the new class of eigenmodes that appears with a wind stress two and a half times stronger than the climatological value. More details are given by Ferjani (2013).

To examine the sensitivity of the least damped basin mode to the forcing type and magnitude, several numerical experiments have been carried out. Comparisons are made in terms of vertical velocities induced by either the diapycnal flux $w_I$ or the Ekman pumping $w_E$. The results show an overall decrease of the damping rate for increasing forcing
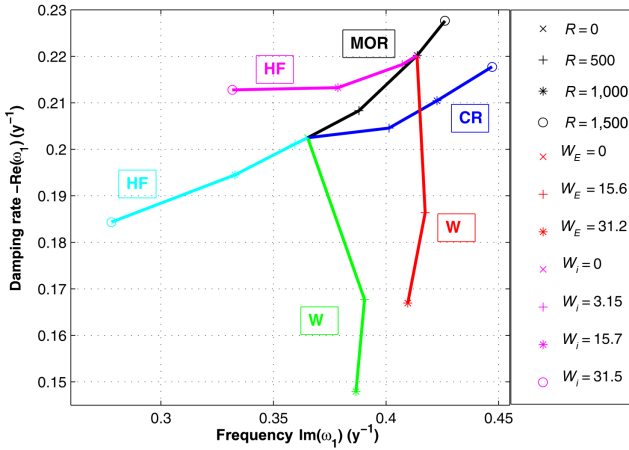
Figure 7. Sensitivity diagram in the $\omega_i - \omega_r$ plane of the least damped basin mode eigenvalue to different prescribed topography shapes (flat bottom, midocean ridge [MOR]) and heights (from 0 to 1,500 m), as well as various forcing types (wind, W; heat flux, HF) and magnitudes (from 0 to approximately 31 m y$^{-1}$). The CR eigenvalue branch corresponds to the continental rise—bottom shape discussed by Ferjani *et al.* (2013). The gradual increase of the wind (red) and heat flux (magenta) magnitudes in the presence of MOR is the same as with a flat bottom: wind (green) and heat flux (cyan).

independently of its type (Fig. 7). However, they exhibit a different behavior of the oscillation period depending this time on the forcing type, with a shortening (lengthening) in the case of wind (thermal) forcing.

### a. Oscillation period

Through a scaling analysis, we try to rationalize the oscillation period evolution for the two types of forcing. As demonstrated in the previous section, the net zonal perturbation advection mechanism is controlled by $c_R + \overline{u^+}$, where the sign and magnitude of the mean flow modify the velocity at which the variability signal propagates westward as planetary Rossby waves, at the speed $c_R$. A reference value for the period has been proposed by Cessi and Louazel (2001) as the time it takes for the long Rossby waves to cross the basin along the northernmost boundary. We propose hereafter a slight modification to this estimation, by using the long Rossby wave speed at the latitude of the maximum amplitude of the eigenmode: This works quite accurately for the rest-state modes, where using $c_R = -0.013$ m s$^{-1}$ (Fig. 8d) leads to an oscillation period of 16.1 y (vs. 17.2 y for the flat and 15.2 y for MOR eigenmodes). It then follows that the oscillation period is now set by the basin zonal extent divided by the residual advection, defined as westward long Rossby wave speed $c_R$ plus the mean barotropic zonal flow $\overline{u^+}$, both estimated at the latitude of the maximum amplitude of the eigenmode, based on the actual mean state.
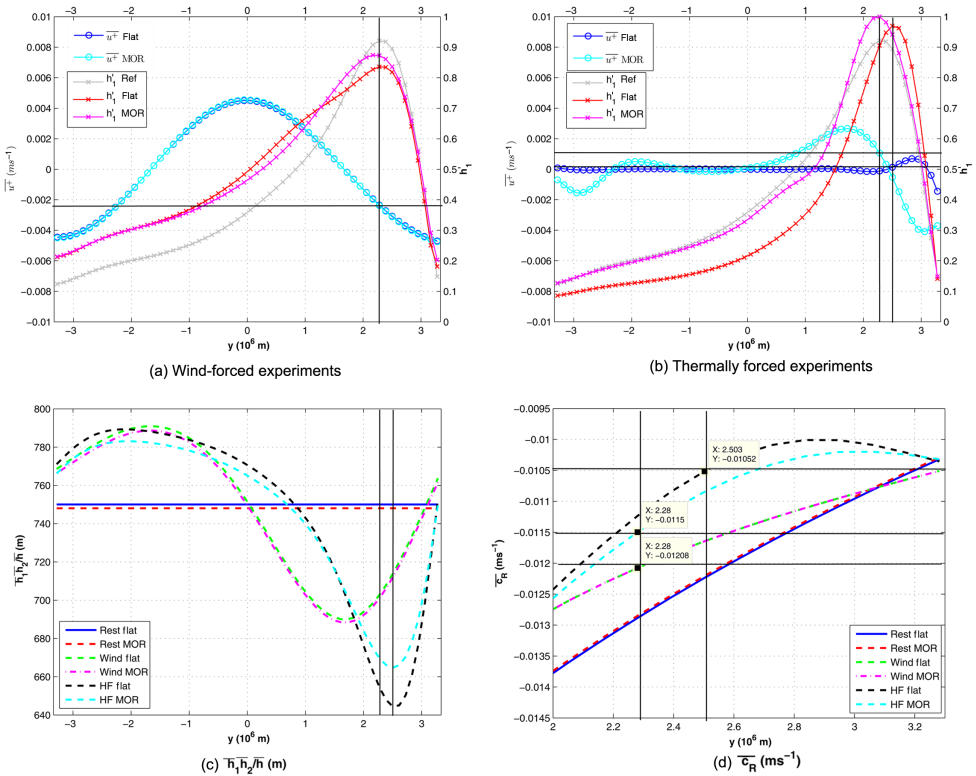
Figure 8. Zonally averaged mean barotropic zonal flow with (cyan) and without (blue) topography, and meridional pattern of the least damped basin mode with (magenta) and without (red) topography, for the climatological wind-forced (a) and thermally forced (b) background circulation. Note the overlapping lines for the wind-forced flow with (cyan) and without (blue) topography. The meridional signature of the reference mode (without background flow) is added in gray for comparison. (c) Meridional variation of the zonally averaged equivalent depth of the background states $\overline{h^*} = \overline{h_1 h_2 / h}$ (m). (d) Zoom in on the zonally averaged long planetary Rossby wave speed in the northern part of the subpolar gyre for the different scenarios of forcing and topography. Black solid lines localize the maximum of the zonally averaged modes amplitude ($h_1'$). HF, heat flux; MOR, midocean ridge.

*i. Wind-forced Sverdrup flow case.* Figure 8 illustrates the meridional distribution of the variability pattern (crossed line) and the zonal mean barotropic flow advection $\overline{u^+}$ (circled line) for the climatologically forced experiments, in order to determine the value of the mean flow at the location of the maximum variability of the least damped basin mode. In the wind-forced experiments, we note the close vicinity of the eastward barotropic jet flowing at the junction between the two antisymmetric gyres to the null-Ekman-pumping line. Note also that the eastward extension of the corresponding least damped basin mode amplitude over a flat bottom appears smaller than the one with a variable-bottom topography (Fig. 9):
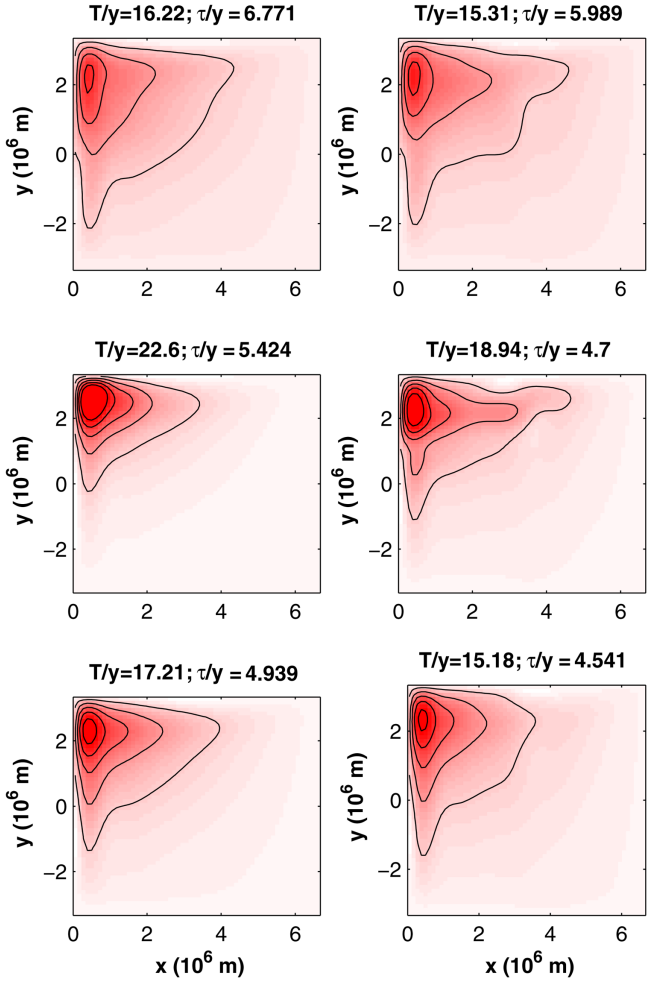
Figure 9. Least damped basin mode amplitude $\sqrt{X_r^2 + X_i^2}$ as expressed in terms of the upper-layer thickness anomaly $h_1'$: flat-bottom experiment (left); 1,000 m midocean ridge experiment (right). Top panels correspond to the climatological wind forcing; middle panels, the thermal forcing; and bottom panels, the rest state.

This agrees with the idea discussed by Tailleux and McWilliams (2000) and Ferjani, Huck, and de Verdière (2013) of the increase of the variability signal amplitude over the bottom relief when propagating westward (Fig. 10). The first two amplitude maxima fall almost at the same meridional location (Fig. 8c), implying very close values of zonal advection (approximately $-2 \times 10^{-3}$ m s$^{-1}$), modifying the planetary Rossby waves phase speed taken at the same location ($-1.2 \times 10^{-2}$ m s$^{-1}$), such that the net advection ($-1.4 \times 10^{-2}$ m s$^{-1}$) leads to a theoretical oscillation period of 14.9 y, reasonably close to numerical mode
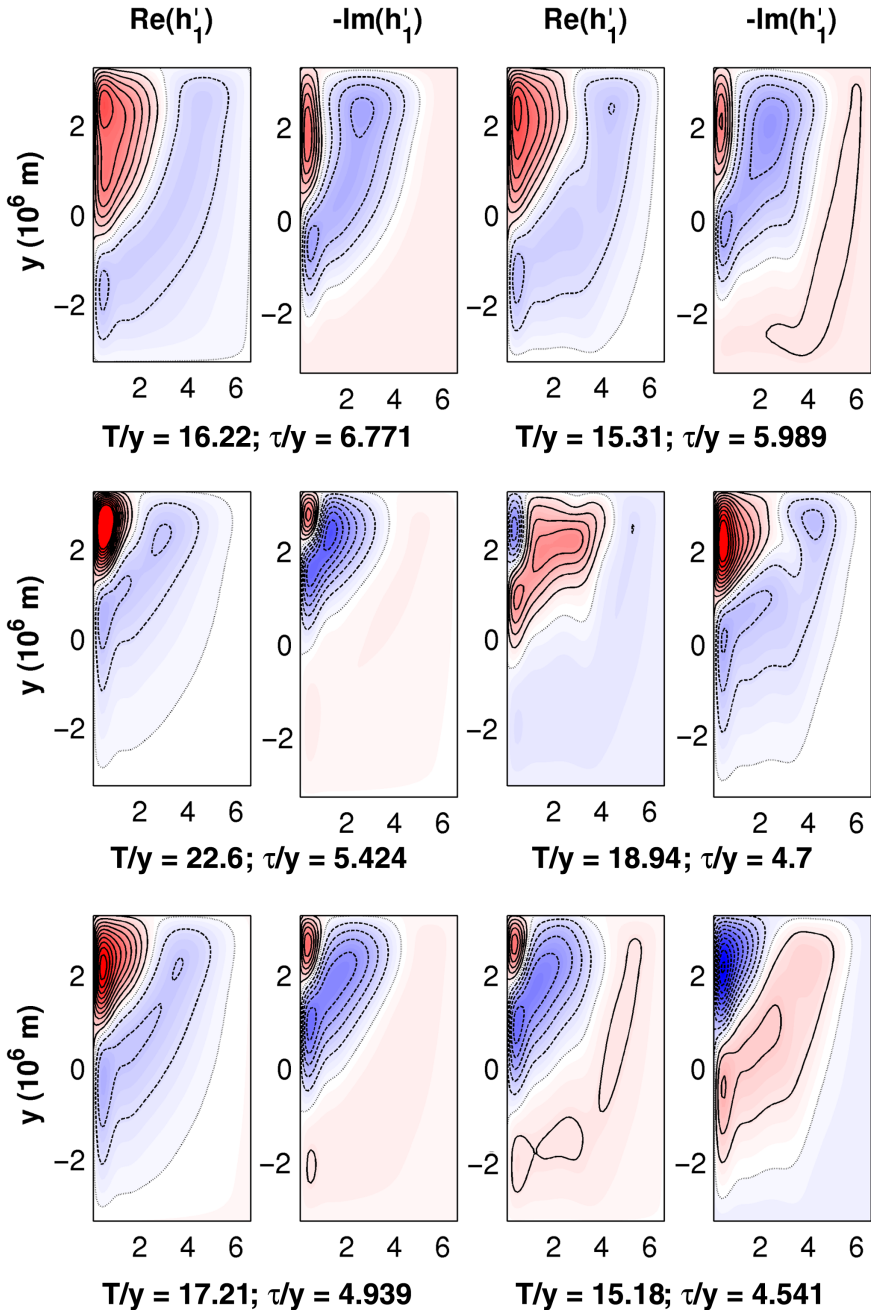
Figure 10.  Real and negative of the imaginary parts of the least damped basin mode as expressed in terms of the upper-layer thickness anomaly $h'_1$: flat-bottom experiment (left); 1,000 m midocean ridge experiment (right). Top panels correspond to the climatological wind forcing; middle panels, the thermal forcing; and bottom panels, the rest state. The x-axis is in $10^6$ m. The time evolution of the mode is $Re(h'_1) \rightarrow -Im(h'_1) \rightarrow -Re(h'_1) \rightarrow Im(h'_1)$ every quarter period and exhibits a westward propagation.

period of 16.2 y. In this case, the mean flow brings a slight acceleration to the westward propagation of the variability signal, which overcompensates the reduction in the Rossby wave speed $c_R$ due to the shoaling isopycnals poleward: this finally results in a shorter oscillation period with respect to the reference case (17.2 y). Besides, both in the presence or not of a variable-bottom topography, the oscillation period of the least damped basin mode is not significantly influenced by the wind forcing, whose action does not reach the bottom layer, as attested by the evolution of the corresponding eigenvalues (Fig. 7).

*ii. Baroclinic thermal-forcing case.* The same rationale holds for the case of a baroclinic forcing exerted at the base of the thermocline. The eastward advection by the mean barotropic flow is drastically shifted to the north in the presence of a meridional downsloping isopycnals due to the mass sink in the subpolar gyre, compared with the wind-forced experiment. The mean barotropic advection is found to be positive both in the presence or not of bottom topography, although almost nonexistent in the flat-bottom case. The planetary Rossby waves speed is thus slowed in the northern half of the basin, leading to a lengthening of the thermal-forcing mode period, in good agreement with the form of the eigenvalue evolution branch in Figure 7. For instance, for the flat-bottom climatological-forcing experiment, $\overline{u^+}$ is O($+2 \times 10^{-4}$ m s$^{-1}$) while the westward planetary Rossby waves speed $c_R$ is O($-1.05 \times 10^{-2}$ m s$^{-1}$), giving a net residual advection of O($-1.03 \times 10^{-2}$ m s$^{-1}$) coincident with a period of about 20.3 y. This theoretical estimate falls fairly close to the numerical oscillation period of 22.6 y (Table 2).

In the presence of an MOR under thermodynamic forcing, the eastward barotropic advection is strongly shifted to the north, in contrast with the wind-forced case in which the eastward advection is located at the intergyre around the line of vanishing Ekman pumping (see $\overline{u^+}$MOR in Fig. 8b vs. Fig. 8a). In addition to the reduction in the Rossby wave speed due to the shoaling of the isopycnals poleward ($c_R = -1.15 \times 10^{-2}$ m s$^{-1}$), the mean barotropic advection $\overline{u^+}$ is O($+10^{-3}$ m s$^{-1}$), such that the westward propagation of perturbations is significantly slowed ($-1.05 \times 10^{-2}$ m s$^{-1}$) inducing a longer thermocline adjustment of 19.9 y, to be compared with the numerical mode period of 18.9 y. In this case, both processes prove to be equally critical for the change in the oscillation period.

*b. Decay rate*

One plausible explanation for the orthogonality of the two eigenvalue branches depicted in Figure 7 (wind and heat forcing, respectively) stems from the sign of each forcing in the northern half of the basin where the variability signal is concentrated. To understand this result, we recall the equation of conservation of the thermocline thickness. If we consider the subpolar gyre established by the wind-forced experiment, the Ekman pumping velocity $w_E$ that acts at the base of the mixed layer is positive. This upward motion causes stretching in the vertical so that the horizontal motion is convergent. For exactly geostrophic motion, the convergence is proportional to $v$. The horizontal component is toward colder water in

the northern part of the basin, thus giving a warming tendency that enhances the magnitude of the temperature perturbation. The result then follows from the hydrostatics; that is, the ocean warms and expands, so the perturbation pressure is positive and the perturbation layer thickness is enhanced.

This argument gives some insight about the decay rate decrease of the decadal basin mode in the wind-forced experiments and proves to hold for the thermally driven simulations in which $w_I$ exerted at the base of the thermocline is negative in the subpolar gyre. Huck, Vallis, and de Verdière (2001) proposed a similar rationale in terms of upper temperature vertical advection to explain the damping role of upward Ekman pumping on decadal basin modes in continuously stratified planetary geostrophic models. The most fundamental result of this series of experiments is the damping rate decrease of the decadal mode in the presence of a mean flow, both observed in the flat and variable ocean floor. The least damped basin mode in Figure 9 is a coherent pattern robust to the damping effect of both bottom topography and frictional processes whose dissipative effect is partially compensated by the addition of a stationary forcing.

## 5. Discussion and conclusions

In this article, we have addressed the sensitivity of the low-frequency basin modes to a background mean flow, either wind or thermally forced, in the presence or not of bottom topography. From a basic scaling analysis, the oscillation period varies as a function of the model parameters in good agreement with the zonal extent of the basin divided by the zonal propagation velocity, which is now classical planetary baroclinic Rossby waves modified by the mean stratification and the barotropic mean flow.

The potential effect of topography is the damping of the gravest baroclinic mode, in agreement with other previous works (Greatbatch, Peterson, and Roth 1997; Winton 1997). The damping is found to be sensitive to the form of the topographic features but remains smaller than frictional dissipation at first order even with large-amplitude topography (Ferjani, Huck, and de Verdière 2013). We also observed an intensification of the mode amplitude over the bottom relief (Fig. 9). With the addition of a mean flow, the interdecadal basin modes appear less damped with realistic forcing magnitudes. The characteristic time of the adjustment process in presence of a steady mean flow is found to be influenced by two main processes: the change in Rossby wave speed $c_R$ due to changes in the mean state stratification and the meridional shift of the eastward barotropic advection, providing a reasonable rationale for the oscillation period found in the numerical experiments.

The emergence of a new class of basin modes referred to as "pool modes" by Spydell and Cessi (2003), Ben Jelloul and Huck (2005), and Ferjani (2013), and trapped within closed geostrophic contours that correspond to region where the general PV Rossy waves are arrested by the mean flow, was not observed in the climatological-forcing range. Nevertheless, this might occur in the region of the Gulf Stream–like eastward flow, in which case, a new parameter regime should be explored to zoom in on the dynamics in this region of intense baroclinic instability.

The conclusions of this study agree with previous works (e.g., Huck, Vallis, and de Verdière 2001) related to the robustness of the decadal-scale variability associated with basin modes regardless of the forcing type, the basin shape, and its bottom irregularities. These results are encouraging as intrinsic oceanic modes are a potential source of decadal variability in the ocean. They can be excited during the geostrophic adjustment to changing winds or buoyancy fluxes and/or instability of the mean flow (de Verdière and Huck 1999). However, in contrast to the findings of Huck and Vallis (2001), no unstable basin modes were observed with our two-layer SW numerical configuration, probably due to the limited number of vertical layers and the absence of outcropping. The large-scale baroclinic instability invoked for spontaneous multidecadal variability of the buoyancy-forced circulation results from higher vertical mode interactions that are not permitted here (there is almost no barotropic flow in these flat-bottom experiments with no wind forcing). The two-layer approximation may be restrictive, and the results will need to be tested in models with greater vertical resolution. We do believe, however, that it is proper to proceed from simple models to more complex ones, both in terms of resolution (more layers in the vertical) and additional physical processes (e.g., mesoscale dynamics, transient winds, bottom-layer outcropping), and that the calculations discussed hereafter can serve as benchmarks for future ones. Preliminary results with a three-layer version of the SW model show good agreement for the influence of the mean flow on basin modes with first baroclinic mode vertical structure; however, the least damped basin modes now have the vertical structure of a second baroclinic mode and are even more influenced by the mean flow intensity due to their slower westward propagation. This points out the importance of increasing the vertical resolution, which is expected to help link the traditional basin modes of Cessi and Primeau (2001) to more realistic decadal variability modes, like those of Buckley et al. (2012) or Tulloch and Marshall (2012) in coupled models, a task left for future investigations.

## APPENDIX

The derivation of equations (10) and (11) uses planetary geostrophy and starts from the continuity in the lower layer:

$$\partial_t h_2 + \nabla \cdot (h_2 \mathbf{u_2}) = 0, \tag{A1}$$

which can be expressed in terms of vertical displacement of the layer interface $\eta_2$ and topography $b$ as

$$\partial_t \eta_2 + h_2 \nabla \cdot \mathbf{u_2} + \mathbf{u_2} \cdot \nabla(\eta_2 - b) = 0. \tag{A2}$$

The divergence term is now eliminated with the help of the lower-layer vorticity conservation (equation 6) to give

$$\partial_t \eta_2 - \frac{\beta}{f} h_2 v_2 + \mathbf{u_2} \cdot \nabla \eta_2 - \mathbf{u_2} \cdot \nabla b = 0. \tag{A3}$$

The planetary geostrophic equations reduce to $f\mathbf{k} \times \mathbf{u_1} = -g\nabla \eta_1$ and $f\mathbf{k} \times \mathbf{u_2} = -g\nabla \eta_1 - g'\nabla \eta_2$, assuming that $\eta_2 \gg \eta_1$. It follows that the thermal wind can be expressed as $f\mathbf{k} \times (\mathbf{u_2} - \mathbf{u_1}) = -g'\nabla \eta_2$ implying $(\mathbf{u_2} - \mathbf{u_1}) \cdot \nabla \eta_2 = 0$. Introducing this into equation (A3) gives equation (8).

Equation (10), which describes the temporal evolution of the barotropic motion, is now obtained by summing equations (7) and (8). The resulting equation reads

$$\partial_t \eta_1 - \frac{\beta}{f} (h_1 v_1 + h_2 v_2) - \mathbf{u_2} \cdot \nabla b = 0. \tag{A4}$$

The lower-layer velocity is then substituted in equation (A4) by its barotropic and baroclinic components (i.e., $\mathbf{u}^+ - \frac{h_1}{h}\mathbf{u}^-$), in the last term:

$$\partial_t \eta_1 - \frac{\beta}{f} h v^+ - \mathbf{u}^+ \cdot \nabla b + \frac{h_1}{h}\mathbf{u}^- \cdot \nabla b = 0. \tag{A5}$$

Finally, substituting the baroclinic velocity $\mathbf{u}^- = -g'/f\mathbf{k} \times \nabla \eta_2$ in equation (A5) gives equation (10).

Similarly, let us consider the continuity in the upper layer:

$$\partial_t (\eta_1 - \eta_2) - \mathbf{u_1} \cdot \nabla \eta_2 - \frac{\beta h_1}{f} v_1 = 0, \tag{A6}$$

in which we replace the upper-layer velocity with its barotropic and baroclinic components and use $\mathbf{u}^- \cdot \nabla \eta_2 = 0$ to get

$$\partial_t (\eta_2 - \eta_1) + \mathbf{u}^+ \cdot \nabla \eta_2 + \frac{\beta}{f} h_1 v_1 = 0. \tag{A7}$$

At this point, the vertical excursion of $\eta_1$ is safely neglected with respect to $\eta_2$, and the upper velocity in the last term is further decomposed as $\mathbf{u}^+ + \frac{h_2}{h}\mathbf{u}^-$, so the equation becomes

$$\partial_t \eta_2 + \mathbf{u}^+ \cdot \nabla \eta_2 + \frac{\beta}{f}\frac{h_1 h_2}{h} v^- + \frac{\beta}{f} h_1 v^+ = 0. \tag{A8}$$

The final form of equation (11) is recovered once the last term in equation (A8) is replaced by its geostrophic expression, $v^- = -g'/f\, \partial_x \eta_2$, to give

$$\partial_t \eta_2 + \mathbf{u}^+ \cdot \nabla \eta_2 + c_R \partial_x \eta_2 + \frac{\beta}{f} h_1 v^+ = 0, \tag{A9}$$

where $c_R = -\frac{g'\beta}{f^2}\frac{h_1 h_2}{h}$ is the nonlinear phase speed of the baroclinic Rossby wave in a two-layer basin.

REFERENCES

Ben Jelloul, M., and T. Huck. 2003. Basin-mode interactions and selection by the mean flow in a reduced-gravity quasigeostrophic model. J. Phys. Oceanogr., *33*, 2320–2332.

Ben Jelloul, M., and T. Huck. 2005. Low-frequency basin modes in a two-layer quasigeostrophic model in the presence of a mean gyre flow. J. Phys. Oceanogr., *35*, 2167–2186.

Buckley, M. W., D. Ferreira, J.-M. Campin, J. Marshall, and R. Tulloch. 2012. On the relationship between decadal buoyancy anomalies and variability of the Atlantic meridional overturning circulation. J. Clim., *25*, 8009–8030.

Cessi, P., and S. Louazel. 2001. Decadal oceanic response to stochastic wind forcing. J. Phys. Oceanogr., *31*, 3020–3029.

Cessi, P., and F. Primeau. 2001. Dissipative selection of low frequency modes in a reduced-gravity basin. J. Phys. Oceanogr., *31*, 127–137.

Delworth, T. L., and M. E. Mann. 2000. Observed and simulated multidecadal variability in the Northern Hemisphere. Clim. Dyn., *16*, 661–676.

Deser, C., and M. L. Blackmon. 1993. Surface climate variations over the North Atlantic Ocean during winter: 1900–1989. J. Clim., *6*, 1743–1753.

de Verdière, A. C., and T. Huck. 1999. Baroclinic instability: An ocean wavemaker for interdecadal variability. J. Phys. Oceanogr., *29*, 893–910.

de Verdière, A. C., and R. Tailleux. 2005. The interaction of a baroclinic mean flow with long Rossby waves. J. Phys. Oceanogr., *35*, 865–879.

Dewar, W. K. 1987. Planetary shock waves. J. Phys. Oceanogr., *13*, 470–482.

Eden, C., and D. Olbers. 2010. Why western boundary currents are diffusive: A link between bottom pressure torque and bolus velocity. Ocean Modell., *32*, 14–24.

Ferjani, D. 2013. Variabilité décennale de la circulation océanique et modes de bassin: Influence de la topographie et de la circulation moyenne. Ph.D. diss. Brest, France: Ecole doctorale des sciences de la mer, Université de Bretagne Occidentale.

Ferjani, D., T. Huck, and A. Colin de Verdière. 2013. Influence of bottom topography on large-scale decadal basin modes. J. Mar. Res., *71*, 289–316.

Greatbatch, R. J., K. A. Peterson, and H. Roth. 1997. Interdecadal Variability in a Coarse Resolution Model with North Atlantic Bottom Topography. Technical report. Halifax, Nova Scotia, Canada: Department of Oceanography, Dalhousie University.

Hansen, D. V., and H. F. Bezdek. 1996. On the nature of decadal anomalies in North Atlantic sea surface temperature. J. Geophys. Res.: Oceans, *101*, 8749–8758.

Held, I. M. 1983. Stationary and quasi-stationary eddies in the extratropical troposphere: Theory, *in* Large Scale Dynamical Processes in the Atmosphere. B. Hospins and R. P. Pearce, ed. London: Academic Press, 127–168.

Holland, W. R. 1978. The role of mesoscale eddies in the general circulation of the ocean—numerical experiments using a wind-driven quasi-geostrophic model. J. Phys. Oceanogr., *8*, 363–392.

Huang, R. X. 1986. Numerical simulation of wind-driven circulation in a subtropical/subpolar basin. J. Phys. Oceanogr., *16*, 1636–1650.

Huck, T., and G. K. Vallis. 2001. Linear stability analysis of the three-dimensional thermally-driven ocean circulation: Application to interdecadal oscillations. Tellus A, *53*, 526–545.

Huck, T., G. K. Vallis, and A. C. de Verdière. 2001. On the robustness of the interdecadal modes of the thermohaline circulation. J. Clim., *14*, 940–963.

Klocker, A., and D. P. Marshall. 2014. Advection of baroclinic eddies by depth mean flow. Geophys. Res. Lett., *41*, 3517–3521.

Kushnir, Y. 1994. Interdecadal variations in North Atlantic sea surface temperature and associated atmospheric conditions. J. Clim., *7*, 141–157.

LaCasce, J. H. 2000. Baroclinic Rossby waves in a square basin. J. Phys. Oceanogr., *30*, 3161–3178.

LaCasce, J. H., and J. Pedlosky. 2002. Baroclinic Rossby waves in irregular basins. J. Phys. Oceanogr., *32*, 2828–2847.

Lehoucq, R. B., D. C. Sorensen, and C. Yang. 1998. ARPACK Users' Guide. Solutions of Large-Scale Eigenvalue Problems with Implicitly Restarted Arnoldi Methods. Philadelphia, PA: SIAM, 142 pp.

Levitus, S. 1989. Interpentadal variability of temperature and salinity of intermediate depths of the North Atlantic Ocean 1970–1974 versus 1955–1959. J. Geophys. Res.: Oceans, *94*, 6091–6131.

Liu, Z. 1999. Planetary waves modes in the thermocline: Non-Doppler-shift mode, advective mode and Green mode. Q. J. R. Meteorol. Soc., *16*, 1315–1339.

Primeau, F. 2002. Long Rossby wave basin-crossing time and the resonance of low-frequency basin modes. J. Phys. Oceanogr., *32*, 2652–2665.

Reverdin, G., D. Cayan, and Y. Kushnir. 1997. Decadal variability of hydrography in the upper northern North Atlantic in 1948–1990. J. Geophys. Res.: Oceans, *102*, 8505–8531.

Sakamoto, T., and T. Yamagata. 1997. Evolution of baroclinic planetary eddies over a localized bottom topography in terms of JEBAR. Geophys. Astrophys. Fluid Dyn., *84*, 1–27.

Schopp, R. 1988. Spinup toward communication between large oceanic subpolar and subtropical gyres. J. Phys. Oceanogr., *18*, 1241–1259.

Spydell, M., and P. Cessi. 2003. Baroclinic modes in a two-layer basin. J. Phys. Oceanogr., *33*, 610–622.

Sutton, R. T., and M. R. Allen. 1997. Decadal predictability of North Atlantic sea surface temperature and climate. Nature, *388*, 563–567.

Tailleux, R., and J. C. McWilliams. 2000. Acceleration, creation, and depletion of wind-driven baroclinic Rossby waves over an ocean ridge. J. Phys. Oceanogr., *30*, 2186–2213.

Tulloch, R., and J. Marshall. 2012. Exploring mechanisms of variability and predictability of Atlantic meridional overturning circulation in two coupled climate models. J. Clim., *25*, 4067–4080.

Veronis, G. 1978. Model of world ocean circulation: III. Thermally and wind-driven. J. Mar. Res., *36*, 1–44.

Weijer, W., E. Muñoz, N. Schneider, and F. Primeau. 2013. Pacific decadal variability: Paced by Rossby basin modes? J. Clim., *26*, 1445–1456.

Winton, M. 1997. The damping effect of bottom topography on internal decadal-scale oscillations of the thermohaline circulation. J. Phys. Oceanogr., *27*, 203–208.

Yang, H., and Z. Liu. 2003. Basin modes in tropical–extratropical basin. J. Phys. Oceanogr., *33*, 2751–2763.